

# Additive Manufacturing of In Situ Metal Matrix Composites



Taban Larimian and Tushar Borkar

## 1 Introduction

Additive manufacturing (AM), also known as three-dimensional printing has recently emerged as a subject of intense worldwide attention. Additive manufacturing is the process of building three-dimensional (3D) objects in a layer form using CAD data. Over the past three decades additive manufacturing has advanced from creating basic models or rapid prototyping into near net shape processes and gradually taking over the conventional methods in production of complex shaped objects [1]. Additive manufacturing is also beneficial in terms of decreasing the lead time and reducing the cost of a production of small number of parts [2]. Advances in the additive manufacturing technology have made it possible to manufacture complex-shaped metal components strong enough for real engineering applications [3–16]. While laser additive manufacturing is becoming more and more important in the context of advanced manufacturing for the future, most of the current efforts are focusing on optimizing the required parameters for processing well-matured alloys from powder feedstock to achieve reproducible properties, comparable to, or better than, their conventionally processed counterparts. However, laser additive manufacturing or processing also opens up a new horizon in terms of processing novel alloys and composites that are difficult to process using conventional techniques. According to the Wohlers Report 2015, the current additive manufacturing market of \$4.1 billion is expected to reach \$21.2 in 5 years [17]. An additive manufacturing system takes a computer generated geometric model as its input and builds the geometry by depositing the constituent materials precisely in a layer-by-layer fashion [1, 17, 18]. There are more than ten AM techniques that have been developed so far, which include electron- beam melting (EBM), selective

---

T. Larimian · T. Borkar (✉)

Mechanical Engineering Department, Cleveland State University, Cleveland, OH, USA

e-mail: [T.Borkar@csuohio.edu](mailto:T.Borkar@csuohio.edu)

laser melting (SLM), stereolithography (SLA), fused deposition modeling (FDM), and digital light processing (DLP), etc. [1, 17–24]. Because of the utilization of the layer-by-layer process, additive manufacturing systems are capable of creating geometrically complex prototypes and products efficiently in small to medium quantities. It is thus best suited for applications requiring complex, high value, time-sensitive, and customized products such as automobile and aerospace parts (i.e. complex designs), broken part replacement (i.e. time-sensitive), and medical implants (i.e. highly customized) such as replacement hip joints. This chapter mainly focused on processing of in situ metal matrix composites via laser additive manufacturing processes such as laser engineered net shaping (LENS)- directed energy deposition type AM process and selective laser melting (SLM)- powder bed fusion type AM process.

The LENS<sup>TM</sup> process, in recent years, is having a strong impact on the rapid prototyping, small scale fabrication, and repair of complex parts in industry. Originally, the LENS<sup>TM</sup> process was developed at Sandia National Laboratories and subsequently commercialized by Optomec Design Company. LENS<sup>TM</sup> process uses focused laser beam for melting the metallic powders and 3-D CAD files for designing the solid 3-D object prior to fabrication. LENS<sup>TM</sup> is a freeform additive manufacturing (AM) process for near-net shaping of nearly fully dense, homogeneous bulk materials. The process begins with a computer aided design (CAD) file of a 3-dimensional (3D) component, which is sliced into a series of layers with a predetermined layer spacing/thickness on the order of 0.01 in (0.25 mm). Each layer contains a tool path, which is followed by the multi-axis stage, while pre-alloyed or blends of elemental powders are injected into a melt pool produced by a high-powered laser. The process continues via the sequential deposition of layers to develop the overall 3D shape of the component. Most of the worldwide research and development activities related to additive manufacturing, or 3D printing as it is often referred to, of metallic systems have focused on a rather limited set of alloys, such as: stainless steels, certain nickel base superalloys, and conventional titanium alloys. Furthermore, these alloys have all been processed using pre-alloyed powder feedstock with efforts directed to optimizing feedstock characteristics and deposition parameters to achieve additively manufactured components with properties comparable to wrought or conventional thermo-mechanically processed materials. While these efforts are critical in order to establish 3D printing/additive manufacturing as viable technologies for future manufacturing, the potential of these technologies is underexploited for the development and processing of in situ metal matrix composites via additive manufacturing processes.

Controllable microstructure by altering the processing parameters is another advantage that laser additive manufacturing offers. Processing parameters such as energy density, hatch spacing, powder feed rate scanning speed and strategy have tremendous effect on mechanical properties, residual stress and microstructural characteristics such as morphology and grain size [25]. The importance of processing parameters is due to their impact on the melt pool size, cooling rate, thermal gradient and consequently the residual stresses [25]. Two of the most important parameters are laser power and scanning speed. Higher energy along

with lower scanning speed will result in more incident energy which results in lower cooling rate and consequently a coarser microstructure. According to equation below, the energy density can be altered by changing the scanning speed, more energy equals more melted material [26].

$$E_p = \frac{P}{\pi r^2} \frac{2r}{v} \frac{2r}{s}$$

$E_p$  = energy density (J/m<sup>2</sup>).

P = laser power (W).

v = scanning speed (m/s).

s = scan line spacing (m), and.

r = beam radius (m).

Despite the increase in melting, increasing the laser power has one main disadvantage of causing balling defect and dross formation in melt pools and might result in rougher surface finish [27].

## 2 Metal Matrix Composites

There is an increasing demand from aerospace and automotive sectors to develop new advanced materials which contribute to weight savings, improve energy efficiency, withstand harsh structural loadings, and enhanced tribological performances. To attain such special attributes, the material should possess high specific strength, elastic modulus, and stiffness additional to enhanced functional characteristics. Traditionally, metals and alloys were unable to fulfill these demands. Fortunately, development of metal matrix composites (MMCs), a perfect response and promising material, cater to these requirements. Tailorable characteristic and improved properties of MMCs, such as higher specific stiffness and strength, excellent wear resistance, controlled coefficient of thermal expansion, higher fatigue resistance, and better stability at elevated temperature, are now quickly replacing existing metals or their alloys. MMCs comprise of combined properties of metals as matrices (ductility and toughness), and ceramic reinforcements (high modulus and strength) in the form of continuous or discontinuous fibers, whiskers, or particulates. The reason for increasing demand of metal matrix composites for structural applications is mainly due to their exceptional mechanical and physical properties as well as inexpensive reinforcements and isotropic properties [28]. Metal matrix composites have also played a role in reducing the weight in aerospace structures by decreasing the alloy density [29]. The commonly used reinforcement materials are oxides, nitrides and carbides, whereas titanium, magnesium, aluminum, copper and nickel alloys are used as matrix materials [28, 30]. These metal matrix composites are broadly classified as ex-situ and in-situ metal matrix composites based on the nature of reinforcement formation during their fabrication process. During these techniques, ceramic reinforcements were externally added prior to composite fabrication

into the matrix material (which may be in molten or powder form). The main disadvantages of these conventional ex-situ metal matrix composites involve size limitation of reinforcing phase, which is nothing but the starting powder size, interfacial reaction between the reinforcement and matrix, and poor wettability between the reinforcements and the matrix due to surface contamination of reinforcements. The physical and mechanical properties of metal matrix composites are primarily governed by size and volume fraction of reinforcement as well as the nature of the matrix reinforcement interface. The uniform dispersion of fine and thermally stable ceramic particulates in the metal matrix is desirable for achieving optimum mechanical properties of metal matrix composites. This leads to the development of novel in situ metal matrix composites in which precipitates are synthesized in metallic matrix by a chemical reaction between elements or between elements and compounds during the composite fabrication. The in-situ metal matrix composites exhibit many advantages over ex-situ metal matrix composites: (a) In-situ formed reinforcements are thermodynamically stable and lead to less degradation at elevated temperatures; (b) Strong interfacial bonding between the matrix and the reinforcement due to clean matrix-reinforcement interface due to absence of any interfacial reaction between matrix and reinforcement; and (c) Better physical and mechanical properties due to homogeneous dispersion of fine-scale reinforcements into matrix.

In situ formation of reinforcement is the promising fabrication route for processing metal matrix composites in terms of both technical and economic considerations. In situ metal matrix composites have better control over physical and mechanical properties due to their greater control on the size and level of reinforcements, as well as the matrix-reinforcement interface. Mechanical and physical properties of metal matrix composites are mainly governed by properties of the matrix, dispersion of the reinforcement, interfacial bonding between matrix and reinforcement, and finally the processing method. Various processing routes have been developed due to the great potential and widespread applications of these in situ metal matrix composites that involve matrix materials (titanium, nickel, aluminum and copper) and in-situ reinforcements (carbides, nitrides, and borides). Laser Additive processing of in situ metal matrix composites opens up new horizon to process multifunctional monolithic metal matrix composites that are difficult to process via traditional manufacturing processing such as laser cladding. These MMCs have been processed either by in situ reaction between elemental blend powders or by in situ reaction between elemental blend powders and reactive gases (nitrogen, oxygen, etc.) during laser additive processing. The following section discusses few examples of in situ metal matrix composites processed via laser additive manufacturing processes.

## 2.1 In-Situ Reactions Between Elemental Blend Powders

### 2.1.1 Aluminum Matrix Composites: Al-Fe<sub>2</sub>O<sub>3</sub>

As mentioned before, Selective laser melting is a laser based additive manufacturing process which is not only capable of producing fully dense three dimensional parts, but can also be used for achieving in-situ reactions between powder particles [31]. Compare to aluminum and its alloys, Aluminum metal matrix reinforced with alumina and silicon carbide has better properties in terms of higher strength, lighter weight, thermal conductivity, better wear resistance, and stiffness. Therefore aluminum matrix composites are widely used in the aerospace and automotive industries [32, 33]. The mechanical properties of aluminum alloys can be easily tailored by varying the processing conditions such as solidification rate, is another advantage [34, 35, 52]. As compared to conventional processing routes additive manufacturing provides processing flexibility, which helps in achieving refine and uniform distribution of reinforcement (alumina and iron) within aluminum matrix leading towards better mechanical performance [31]. Sasan et al. have processed mixture of aluminum and Fe<sub>2</sub>O<sub>3</sub> to obtain in situ Al<sub>2</sub>O<sub>3</sub> and Fe<sub>3</sub>Al within aluminum matrix [31]. Fe<sub>2</sub>O<sub>3</sub> is an inexpensive reinforcement which can reduce the amount of energy required for the selective laser melting of aluminum matrix composites [36]. The following stoichiometric reaction reveals the fact that laser produces extra heat and activates thermite interactions during SLM processing:  $8\text{Al} + 3\text{Fe}_2\text{O}_3 \rightarrow 2\text{Fe}_3\text{Al} + 3\text{Al}_2\text{O}_3 + \text{heat}$ , in which Al reduces the Fe<sub>2</sub>O<sub>3</sub> [37]. The extra heat produced during the in-situ reaction not only helps to decrease the energy input required to melt powders but also helps in consolidation of the composites powder. Also, Melting pool which plays an important role in process optimization can be extended in comparison to pure aluminum [36]. Figure 1a, b show the effect of Fe<sub>2</sub>O<sub>3</sub> content on the melt pool size for the parts fabricated with the same SLM processing parameters (laser energy and scanning speed).

The Al/5wt.%Fe<sub>2</sub>O<sub>3</sub> composites create smaller molten pool (Fig. 1a) as compared to Al/15wt.%Fe<sub>2</sub>O<sub>3</sub> composites (Fig. 1b) mainly due to the higher heat released from

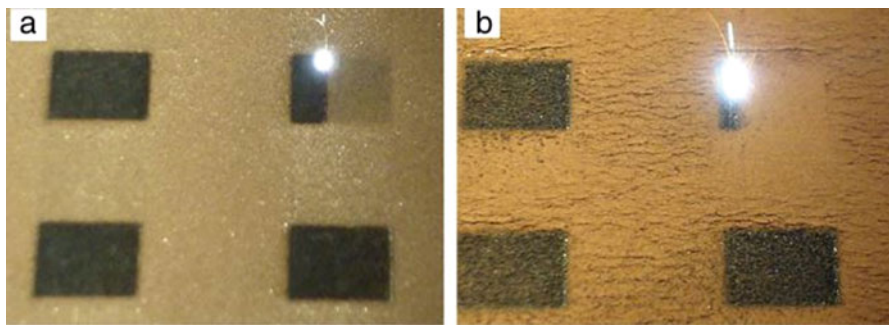


**Fig. 1** The visual appearance of parts being fabricated from (a) Al/5wt.%Fe<sub>2</sub>O<sub>3</sub> and (b) Al/15wt.%Fe<sub>2</sub>O<sub>3</sub> powder mixture using  $P = 82$  W and  $v = 0.33$  m/s. (Reprinted with permission from [36])

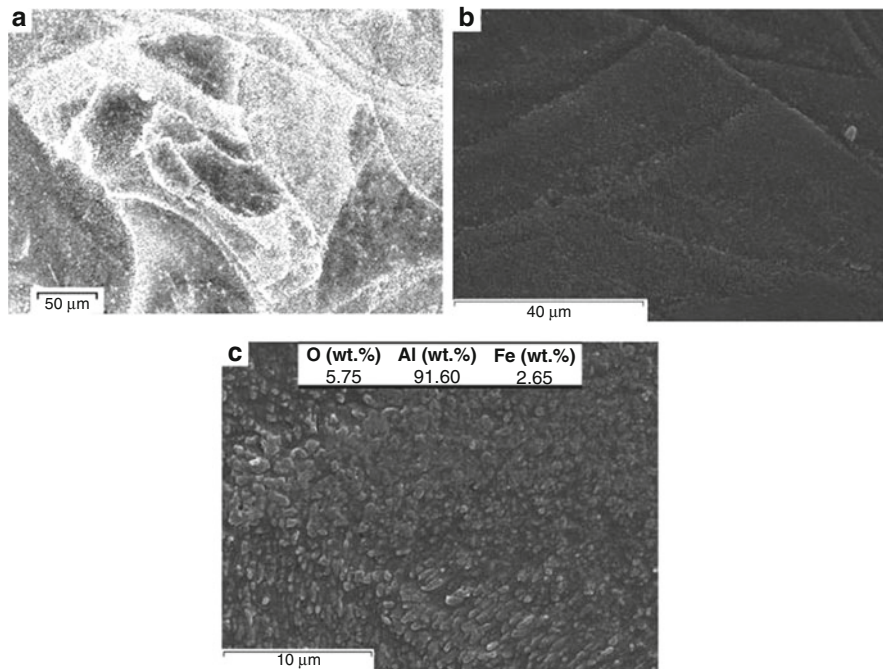
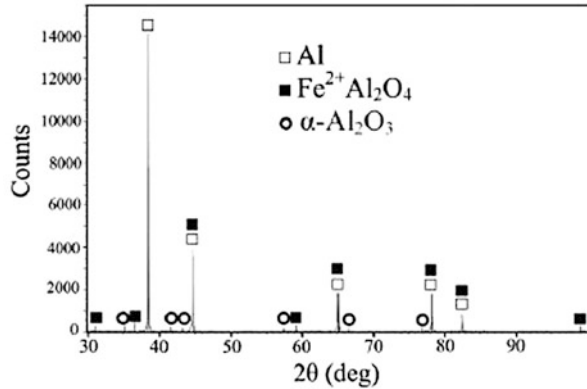


**Fig. 2** Typical microstructural views of the SLM part fabricated from Al/5 wt%  $\text{Fe}_2\text{O}_3$  mixture; (a) Optical microscopy image showing random grain structure, (b) SEM overall view of grain structure and (c) previous image with higher magnification showing fine particles formed inside grains and boundaries (overall chemical composition was acquired by EDS). (Reprinted with permission from [31])

the mixture with higher  $\text{Fe}_2\text{O}_3$  content [36]. Selective laser melting process is capable of producing net-shape aluminum matrix composite parts with uniform properties [31]. The content of  $\text{Fe}_2\text{O}_3$  has significant influence on hardness, density and surface roughness since it can manipulate the amount of energy released in the reaction and subsequently the surface profile. The amount of  $\text{Fe}_2\text{O}_3$  does not have significant effect on the densification of the composites but microhardness significantly increases with increases in  $\text{Fe}_2\text{O}_3$  content. The optical microscopy image of a SLM processed Al- $\text{Fe}_2\text{O}_3$  composites are shown in Fig. 2a, exhibiting random grain structure [31]. Scanning electron microscope (SEM) images shows uniform distribution of fine particles within grains and grain boundaries (Fig. 2b, c). The microstructure shows uniform distribution as well as excellent interfacial bonding of very fine particles (50–2000 nm) within Al matrix which leads to improvement of the mechanical properties of these composites. X-ray diffraction pattern (Fig. 3) confirms the presence of  $\text{Al}_2\text{O}_3$  in these composites which confirms the formation of in situ precipitates during the SLM processing of Al- $\text{Fe}_2\text{O}_3$  composites.

**Fig. 3** The XRD pattern of the SLM sample shown in Fig. 2. (Reprinted with permission from [31])



### 2.1.2 AlSi<sub>10</sub>Mg-SiC

Selecting the proper reinforcement for metal matrix gives the opportunity to design MMCs with better strength and stiffness. Low hardness and poor wear performance of alluminum alloys hinder their use in high temperature surface engineering applications. One way to improve their hardness and wear properties is to reinforce them with hard precipitates such as SiC, Al<sub>2</sub>O<sub>3</sub>, and TiB<sub>2</sub>, due to their good corrosion resistance and high hardness [38–41]. Alluminum matrix composites are widely utilized in aerospace and automotive industries, such as use of fiber reinforced alluminum metal composites by Toyota for their diesel engine pistone or using 25 vol% SiC particulate as reinforcement in 6061 aluminum matrix composite for aerospace applications. In-situ Al<sub>4</sub>SiC<sub>4</sub> + SiC composites have been fabricated via selective laser melting (SLM) of AlSi<sub>10</sub>Mg and SiC powder mixture. Major drawbacks in SLM processing of aluminum matrix composites are the low wettability between the reinforcing particles and the Al matrix, low laser energy absorption by aluminum and its propensity to react with oxygen at high temperatures [42–45]. Fe Cheng et al. have processed in situ Al<sub>4</sub>SiC<sub>4</sub>+ SiC reinforced Al matrix composites via SLM process in order to investigate the effect of starting SiC particle size on densification, microstructure, in-situ reaction, and tribological properties of these composites. Figure 4 shows the XRD patterns of SLM processed Al<sub>4</sub>SiC<sub>4</sub>+ SiC/ Al composites fabricated using different size SiC particles. These results clearly show the effect of SiC particles significantly affects the in situ reaction between Al and SiC during SLM processing. The larger SiC particles leads to weaker Al<sub>4</sub>SiC<sub>4</sub> peaks whereas stronger intensity observed for the composites processed using finer SiC particles. This observation clearly suggests that finer SiC particles enhance the in situ reaction during SLM processing which leads to increase in volume fraction of Al<sub>4</sub>SiC<sub>4</sub>. Reinforcement in Al matrix. Table 1 shows the variation of 2θ position and the Al peak intensities in SLM processed Al<sub>4</sub>SiC<sub>4</sub>+ SiC/ Al composites using different SiC particle sizes. This clearly shows that intensity of Al peaks decreases with reduction in silicon carbide particles size, whereas FWHM increases with decrease in SiC particle size [46, 47]. Since aluminum has a relatively low

**Fig. 4** XRD spectra of SLM-processed  $(Al_4SiC_4 + SiC)/Al$  hybrid reinforced composites with the variation of particle sizes of the starting SiC powder. (Reprinted with permission from [46])

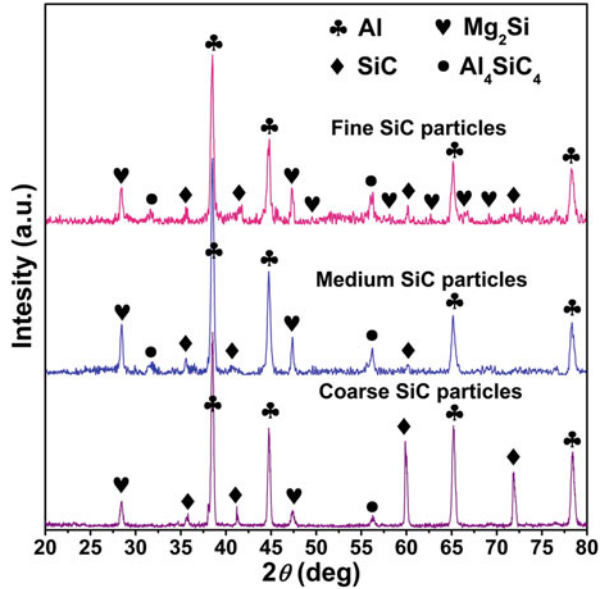


**Table 1** Variation of  $2\theta$  locations and intensities of the Al diffraction peaks in SLM-processed  $(Al_4SiC_4 + SiC)/Al$  hybrid reinforced composites with different SiC particle sizes

Sample	$2\theta$ ( $^\circ$ )	Intensity	FWHM	$2\theta$ ( $^\circ$ )	Intensity	$2\theta$ ( $^\circ$ )	Intensity
Standard	38.47			44.72		65.10	
$D_{50} = 50 \mu m$	38.52	628	0.302	44.74	322	65.28	317
$D_{50} = 15 \mu m$	38.52	492	0.356	44.74	239	65.18	135
$D_{50} = 5 \mu m$	38.50	231	0.387	44.82	116	65.16	86

Adapted from [46]

absorption rate for laser energy, addition of high energy absorptive- silicon carbide particles will help in overall increase in energy absorption rate that leads to form sufficient liquid and more stable molten pools [45, 48]. Furthermore, increase in molten pool's temperature due to increase in the energy absorption rate will result in a better liquid-solid wettability [46]. Size of SiC particles has an effect on density of aluminum matrix composites, since the specific surface area between melt of aluminum and silicon carbide changes with the SiC particle size. The specific surface area between the reinforcement and matrix is limited in the case of coarser SiC particles, consequently the wettability between SiC particles and aluminum matrix decreases leading towards lowering the density SLM processed Al composite. Fine SiC particles help in accelerating the in-situ reaction between matrix and reinforcements which increases their density as well as mechanical properties, improving the density of Al composites [5, 46]. Decreasing the size of SiC particle also enhances the Wear performance and micro hardness of the samples due to higher density and homogenous microstructure. When the SiC is too coarse, less amount of particles



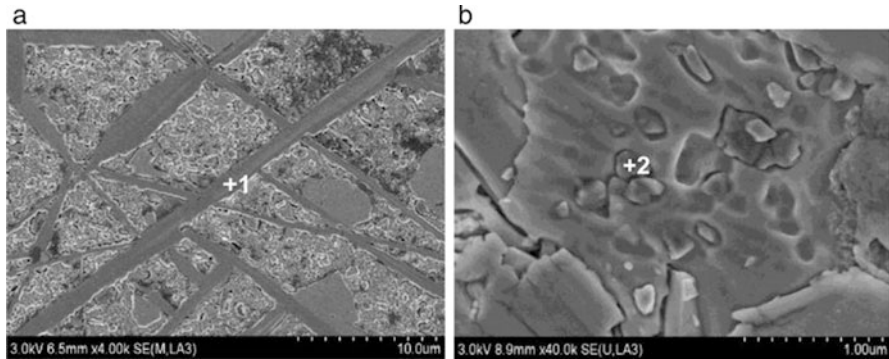


**Fig. 5** FE-SEM images showing the typical morphologies of in-situ reinforcements and the EDX results showing the chemical compositions in SLM-processed ( $\text{Al}_4\text{SiC}_4 + \text{SiC}$ )/Al hybrid reinforced composites using the fine SiC particles: (a) plate-like reinforcement; (b) particle-shaped reinforcement. (Reprinted with permission from [46])

melt during the SLM process, and the interface between SiC particle and Aluminum is insufficient, consequently the in situ reaction between Al and SiC is hindered. Furthermore, residual irregular-shaped SiC particles result in microstructural heterogeneity and a significant decrease in densification level [46]. When the SiC particles are finer, the average size of the remaining SiC particles is smaller and the composite is more homogenous. Two different microstructures of  $\text{Al}_4\text{SiC}_4$  that are created from the in situ reaction between aluminum and SiC micron-sized plate-like structure and nearly nano-sized particle structure shown in Fig. 5 [46]. Process of forming  $\text{Al}_4\text{SiC}_4$  phase during the in-situ reaction between Al and SiC, includes creation of irregular nuclei on the interface of Al and SiC. As the in-situ reaction progresses, these nuclei begin to grow and shape plate-like structures. Homogeneous dispersion of plate-like  $\text{Al}_4\text{SiC}_4$  has a crucial role in enhancing the mechanical properties of the SLM processed parts [46].

### 2.1.3 Nickel Matrix Composites: Ni-Ti-C

Nickel and nickel base superalloys are widely used in aerospace applications (aircraft jet engines, and land base turbines) as well as in land-based applications, including the petrochemical and nuclear energy sectors, due to their excellent properties such as high resistance to corrosion as well as fatigue and low thermal expansion. Titanium carbide (TiC) has a very high hardness (2859–3200 HV), high melting point (3160 °C), low density (4.93 g/cm<sup>3</sup>), and high mechanical strength, but it is very brittle and cannot be used as a monolithic ceramic [49–54]. Therefore, titanium carbide reinforced nickel matrix composites are considered as a good candidate for high temperature refractory, abrasive, and structural as well as surface engineering applications. Also, in contrast to most other metals, nickel exhibits a low wetting angle with titanium carbide, which leads to significant improvements in the

interfacial bonding in titanium carbide reinforced nickel matrix composites. Ni-TiC composites exhibit a good balance of properties combining the ductility and toughness of the nickel matrix with the high strength and modulus of the TiC reinforcement making these composites promising candidates for high temperature structural applications. Furthermore, TiC reinforced nickel matrix composites can also be considered as potential replacements for WC-Co based wear-resistant materials for surface engineering applications. Ni-TiC-C composites exhibited excellent wear resistant properties due to the presence of the graphitic phase, which plays an important role as an in situ solid lubricant during friction. Using laser engineered net shaping (LENS<sup>TM</sup>), novel monolithic composites based on Ni-Ti-C have been developed that combine properties such as solid lubrication (e.g. graphite), high hardness (e.g. TiC), and high fracture toughness (e.g. nickel), for structural as well as surface engineering applications. These multifunctional, monolithic composites are needed in industrial applications, such as drilling components (wear band, stabilizer, drill collar, etc.), tunnel boring, and land base turbines. Laser Engineered Net Shaping (LENS<sup>TM</sup>) provides *processing flexibility*, e.g. in situ composites and functionally graded materials, that traditional laser cladding/hard facing techniques cannot provide. A new class of Ni-Ti-C based metal matrix composites has been developed using the laser engineered net shaping (LENS<sup>TM</sup>) process. These composites consist of an in situ formed and homogeneously distributed titanium carbide (TiC) phase reinforcing the nickel matrix. Additionally, by tailoring the C/Ti ratio in these composites, an additional graphitic phase can also be engineered into the microstructure. The following four types of composites have been processed via LENS<sup>TM</sup> process in order to investigate the effect of excess graphite on microstructure, microhardness, and tribological properties of these composites: Ni-10Ti-5C, Ni-10Ti-10C, Ni-7Ti-20C, and Ni-3Ti-20C. 3D characterization of laser-deposited in situ Ni-Ti-C based metal matrix composites, reveals homogeneously distributed primary and eutectic titanium carbide precipitates as well as a graphitic phase encompassing the primary carbides, within a nickel matrix. The morphology and spatial distribution of these phases in three dimensions reveals that the eutectic carbides form a network linked by primary carbides or graphitic nodules at the nodes, suggesting interesting insights into the sequence of phase evolution. These three-phase Ni-TiC-C composites exhibit excellent tribological properties, in terms of an extremely low coefficient of friction while maintaining a relatively high hardness. Backscattered SEM images of Ni-Ti-C composites with varying C/Ti ratio is shown in Fig. 6. Ni-10Ti-5C (Fig. 6a) composite exhibits only fine needle like eutectic TiC precipitates whereas Ni-10Ti-10C (Fig. 6b) composite shows the presence of both fine needle like eutectic as well as cuboidal primary TiC precipitates. As carbon to titanium ratio increases both Ni-7Ti-20C (Fig. 6c) and Ni-3Ti-20C (Fig. 6d) composites show the presence of black graphite phase along with dark grey TiC precipitates. Ni-7Ti-20C exhibits larger primary TiC precipitates than that of Ni-3Ti-20C mainly because of higher atomic percentage of titanium. The 3D microstructure of Ni-10Ti-10C and Ni-3Ti-20C composites is shown in Fig. 7, where primary (cuboidal shaped) and eutectic (plate-shaped) TiC reinforcements in a

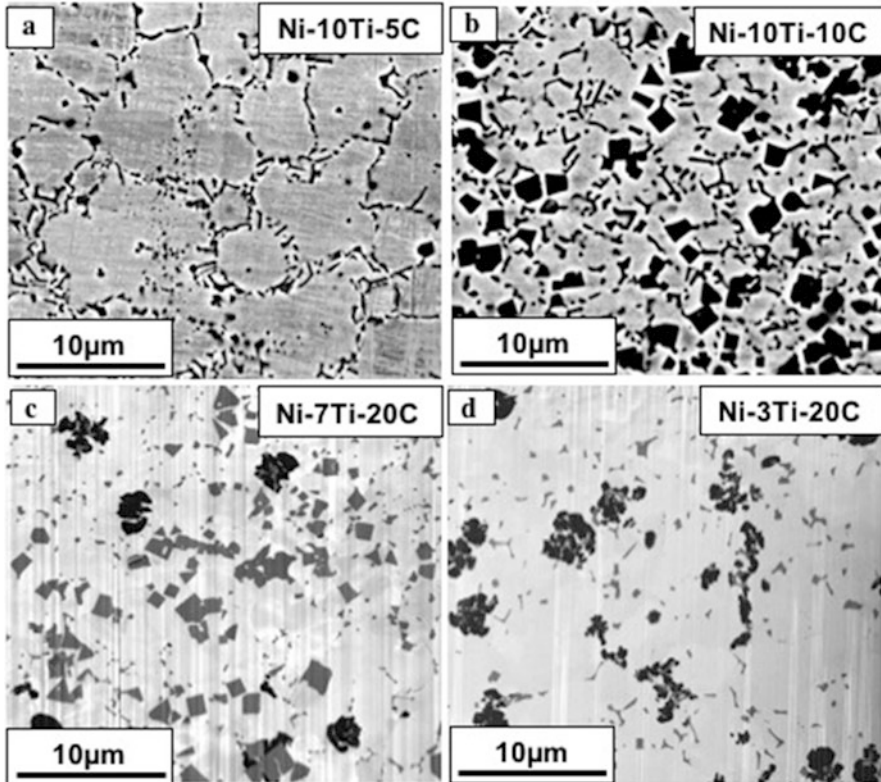


**Fig. 6** Backscatter SEM images of LENS deposited (a) Ni-10Ti-5C, (b) Ni-10Ti-10C, (c) Ni-7Ti-20C, and (d) Ni-3Ti-20C composites. (Modified from [4])

Ni matrix have been reconstructed. 3D microstructural characterization of Ni-Ti-C composites revealed:

- (a) Different morphologies of primary and eutectic TiC precipitates: primary TiC precipitates exhibit a cuboidal morphology whereas eutectic TiC precipitates appear to exhibit a plate-like morphology.
- (b) Primary Graphite phase engulfs TiC precipitates.
- (c) Primary TiC precipitates act as heterogeneous nucleation sites for the eutectic precipitates during solidification leading to a carbide network formation.

3D characterization leads to novel understanding of the sequence of phase evolution during solidification for these complex metal matrix composites. The connectivity between the carbide precipitates is nearly impossible to visualize based on the 2D SEM images shown in Fig. 6. The distinction between the cuboidal primary TiC precipitates and the plate or needle-shaped eutectic TiC precipitates is more difficult in Ni-3Ti-20C composites because the primary precipitates are smaller in size as clearly shown in the 3D reconstruction. The Vickers microhardness values for the Ni-Ti-C composites and pure Ni have been listed in Table 2. Comparing these

**Fig. 7** 3D reconstruction of LENS deposited (a) Ni-10Ti-5C and (b) Ni-3Ti-20C composites. (Modified from [4])

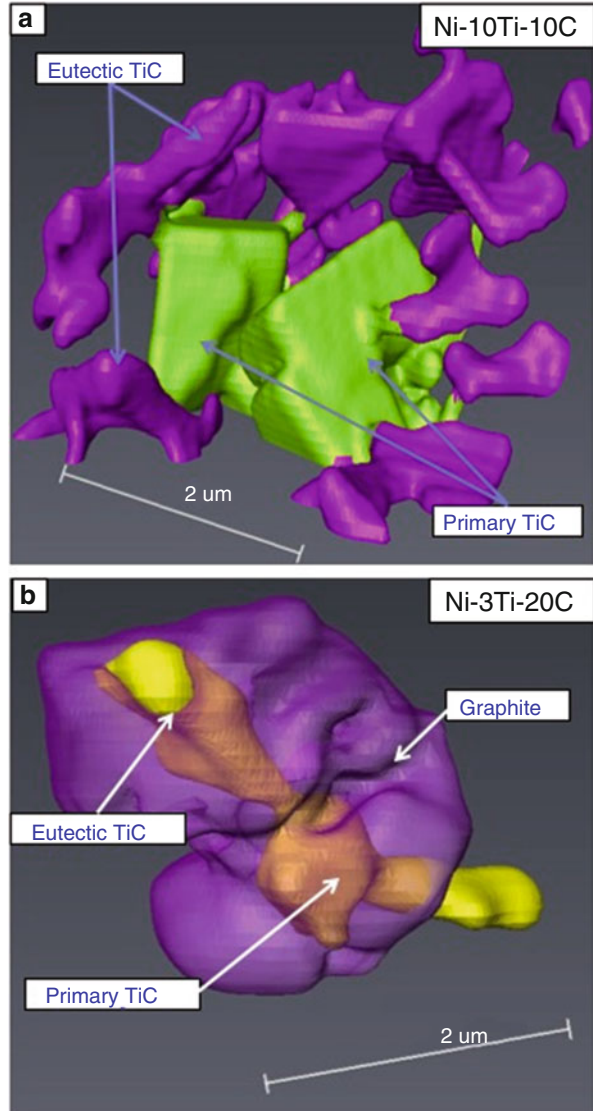
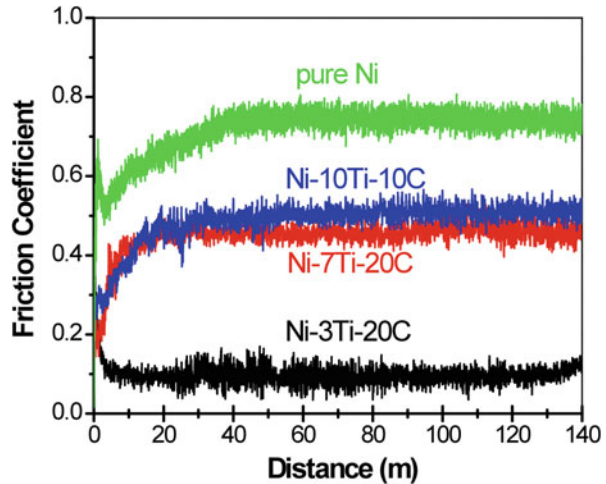


**Table 2** Microhardness of Ni-Ti-C composites

Sample	Hardness (HV)
Pure Ni	165 ± 6
Ni-3Ti-20C	240 ± 6
Ni-7Ti-20C	290 ± 7
Ni-10Ti-10C	370 ± 10
Ni-10Ti-5C	265 ± 2

**Fig. 8** Steady state friction coefficient as a function of sliding distance up to 140 m for LENS deposited pure Nickel, Ni-10Ti-10C, Ni-7Ti-20C, and Ni-3Ti-20C composites. (Modified from [4])



microhardness values, the Ni-10Ti-10C composite exhibited a substantially higher hardness of 370 VHN as compared to 165 VHN for the LENS<sup>TM</sup> deposited pure Ni and all other Ni-Ti-C composites. These microhardness values clearly show a trend of decreasing hardness as a function of increasing C/Ti ratio in the composite. The Ni-10Ti-10C composites exhibit highest hardness mainly due to the presence of high volume fraction of titanium carbides (both primary and eutectic) as compared to pure nickel as well as other Ni-Ti-C composites. Figure 8 shows Friction coefficient versus distance plot LENS<sup>TM</sup> deposited Ni-10Ti-10C, Ni-3Ti-20C, Ni-7Ti-20C composites and pure nickel. It is clear that the graphite and TiC phases in the composite were beneficial towards reducing the friction coefficient with respect to the pure nickel sample. While the presence of TiC reduces the coefficient of friction, as observed in case of the Ni-10Ti-10C composite, the presence of the lubricious graphitic phase can play a more dominant role in reducing the friction for these composites. This is evident from the friction curves for the Ni-7Ti-20C and Ni-3Ti-20C composites. The friction coefficient in case of Ni-7Ti-20C is marginally lower as compared to Ni-10Ti-10C due to the presence of the graphitic phase in the former. However, the most promising composite appears to be the Ni-3Ti-20C composite, which exhibits a drastic reduction in friction coefficient ( $\sim 0.2$ ) when compared to any of the other composites, mainly due to the presence of a substantial fraction of the graphitic phase as well as TiC precipitates. All the Ni-Ti-C composites exhibit very high microhardness as well as excellent tribological properties when compared to pure nickel. The Ni-10Ti-10C composite exhibits highest microhardness due to the presence of primary as well as eutectic TiC precipitates, whereas the Ni-3Ti-20C composite exhibits excellent tribological properties due the presence of solid lubricious graphite phase along with TiC precipitates. Thus, these Ni-Ti-C composites, especially the Ni-3Ti-20C composite, appear to be promising

materials for high temperature surface engineering applications requiring high hardness with improved solid lubrication.

#### 2.1.4 Titanium Matrix Composites: Ti-B and Ti64-BN

Even though in situ metal matrix composites have several advantages over ex situ metal matrix composites, very few researchers have studied in situ metal matrix composites processed via laser additive manufacturing. This section will give the overview of those in situ metal matrix composites processed via laser additive manufacturing Himanshu et al. [55, 56] have performed in situ nitridation of titanium alloys using laser gas nitriding in the laser engineered net shaping (LENS<sup>TM</sup>). There is a significant improvement in microhardness as well as wear resistance observed in those composite coatings due to the presence of TiN and Ti<sub>2</sub>N along with unreacted  $\alpha$ -Ti phase. These nitrided precipitates exhibited dendritic morphology and uniformly distributed within  $\alpha$ -Ti matrix. Das et al. [57, 58] have processed TiB + TiN reinforced composite coatings using Ti-6Al-4 V and hexagonal boron nitride (h-BN) powders via LENS<sup>TM</sup> process. TiB-TiN reinforced Ti64 coatings have been processed with varying BN wt% as well as laser power. The TiN phase exhibits coarse dendritic and needle-like structure whereas TiB phase exhibits fine rod-like structure (Fig. 9). During laser processing BN decomposes and react with molten titanium which give rise to TiB and TiN precipitates. These composite coatings have shown significant improvement in fracture toughness as well as tribological properties as compared to Ti-6Al-4 V alloy. Hooyar et al. [59] have processed Ti-TiB composites via selective laser melting process using milled Ti-TiB<sub>2</sub> powders. SEM images of both cross-sectional and longitudinal sections of SLM processed Ti-TiB composites are shown in Fig. 10. The TiB precipitates exhibit needle-shape morphology and are uniformly distributed within titanium matrix. The Ti-TiB composites have shown significant improvement in microhardness (402 HV) and compressive yield strength (1103 MPa) as compared to SLM-processed CP-Ti (261 HV and 560 MPa). These superior mechanical properties have mainly attributed due to the strengthening and hardening effects of the TiB particles and grain refinement of the  $\alpha$ -Ti matrix. Vamsi et al. [60] have deposited ZrO<sub>2</sub> coatings on titanium substrate using Zr powder via LENS process in Ar + O<sub>2</sub> inert atmosphere. Laser oxidized Zr coatings have shown enhancement in osteoblast cell adhesion as well as in the wear resistance due to the presence of monoclinic as well as tetragonal ZrO<sub>2</sub>. Ti alloy-TiB composites combine the high strength and stiffness of the borides with the toughness and damage tolerance of the Ti-alloy matrix. These composites have been extensively researched since they offer attractive properties, such as: high stiffness, enhanced elevated temperature strength, good creep performance, fatigue resistance and wear resistance. Since the boride reinforcement was formed as a consequence of a chemical reaction in such composites, a homogeneous dispersion consisting of refined scale borides results. Furthermore, the boride phase that forms in these in situ composites is in thermodynamic equilibrium with the matrix. Unlike reinforcement phases added from external

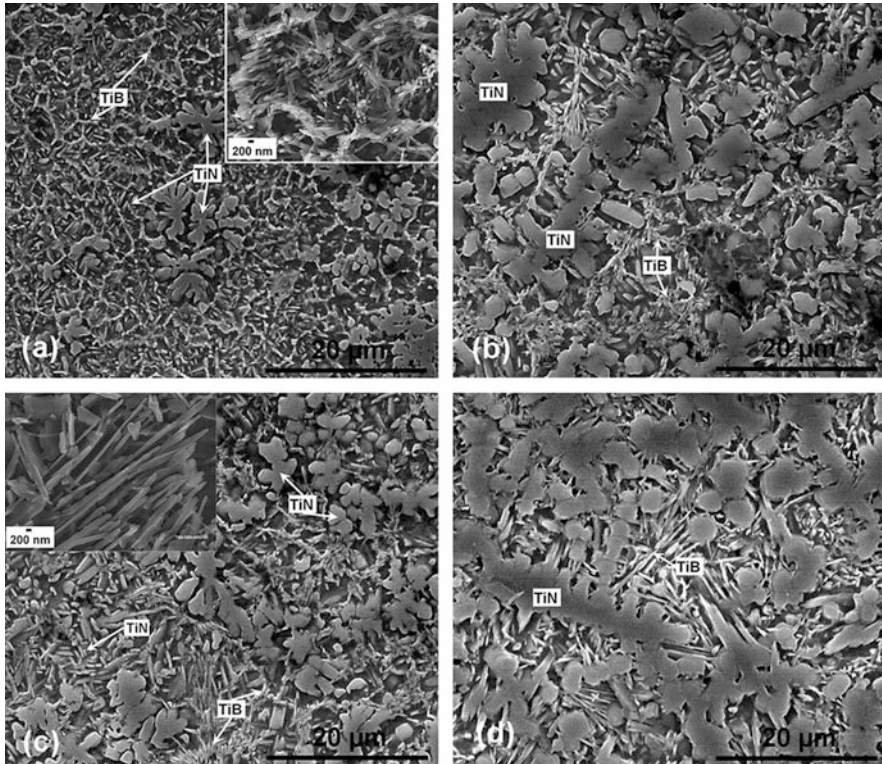


**Fig. 9** Typical high-magnification SEM microstructures showing Ti-BN reactions products in laser-processed, BN-reinforced Ti6Al4V alloy composite coatings: (a) 5BN-300/20 ( $38 \text{ J mm}^{-2}$ ); (b) 15BN-300/20 ( $38 \text{ J mm}^{-2}$ ), (c) 5BN-400/10 ( $102 \text{ J mm}^{-2}$ ), (d) 15BN-400/10 ( $102 \text{ J mm}^{-2}$ ). Inset shows scale of TiB nanorods in respective coatings. (Reprinted with permission from [57])

sources, in situ composites consist of contaminant-free boride-matrix interfaces, which are significantly stronger. Banerjee et al. have processed Ti-TiB composites via the LENS<sup>TM</sup> process from a blend of pure elemental Ti and B powders while Ti alloy-TiB composites were deposited from a blend of pre-alloyed Ti-6Al-4 V and elemental boron [61–64]. The homogeneous dispersion of the fine TiB precipitates achieved in laser deposited Ti alloy-TiB composites deposited using LENS process was expected to significantly strengthen the  $\alpha$ -Ti or  $\alpha/\beta$  Ti-6Al-4 V matrix and consequently holds promise from the viewpoint of enhanced high temperature mechanical properties such as creep as well as wear resistance of these composites. Figure 11 shows the microstructure of LENS<sup>TM</sup> deposited Ti-6Al-4 V-TiB composites. The needle-shaped TiB precipitates are uniformly distributed with titanium matrix. In addition, since these were in situ composites, the reinforcing TiB precipitates were thermodynamically stable at high temperatures, chemically compatible with the matrix, as well as bonded strongly to the matrix due to the clean interface between the matrix and the reinforcement. Sonia et al. have processed *in situ* Ti-Nb-

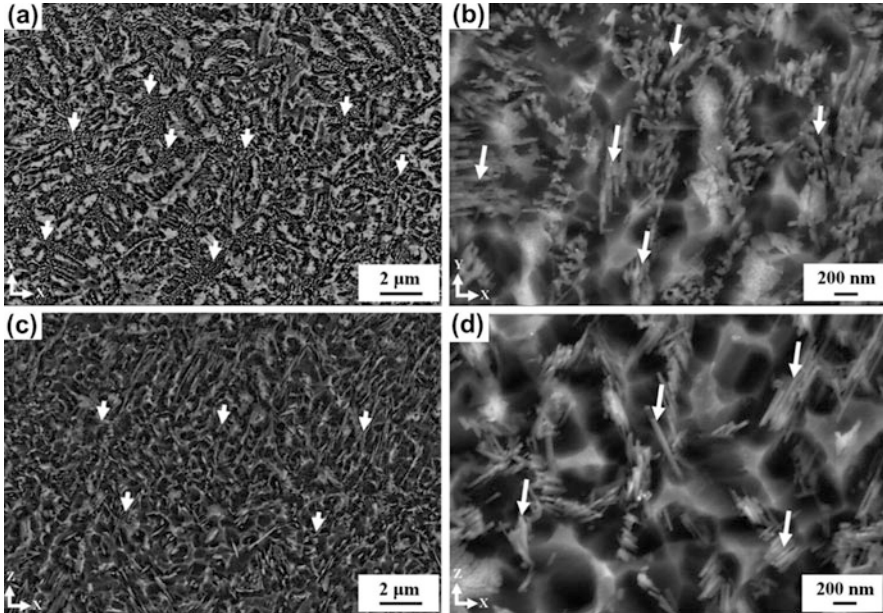


**Fig. 10** SEM images for the microstructures of the SLM-produced Ti–TiB composite at different magnifications: (a, b) cross-sectional views and (c, d) longitudinal views showing needle-shape TiB particles within the Ti matrix. White arrows indicate TiB particles. (Reprinted with permission from [59])

Zr-Ta-TiB composites via LENS<sup>TM</sup> technique from a blend of pure elemental titanium (Ti), niobium (Nb), zirconium (Zr), and tantalum (Ta) powders mixed with titanium diboride (TiB<sub>2</sub>) powders [47, 48]. The microstructure of the LENS<sup>TM</sup>-deposited TNZT+2B alloy at different magnifications is shown in the backscatter SEM images in Fig. 12. Two types of TiB precipitates have been observed within titanium matrix. The coarser precipitates have hexagonal-shaped geometry whereas eutectic TiB precipitates exhibit fine needle-shape morphology. TNZT-TiB composites have shown significant improvement in wear resistance as compared to TNZT alloys.

## 2.2 *In Situ Reaction Between Elemental Blend Powders and Reactive Gases*

### 2.2.1 Ti-Mo-N

Titanium alloys are attractive candidates for structural, marine, aerospace, biomedical (such as in dental and orthopedic as bone implants) and other industrial applications due to their excellent strength to weight ratio, ductility and formability,



**Fig. 11** (a) Backscatter SEM micrograph showing the overall microstructure of the LENS™ deposited Ti-6Al-4 V-TiB composite with TiB precipitates distributed within an  $\alpha + \beta$  matrix. (b) Bright-field TEM micrograph showing two TiB precipitates in the Ti-6Al-4 V matrix. (Reprinted with permission from [64])

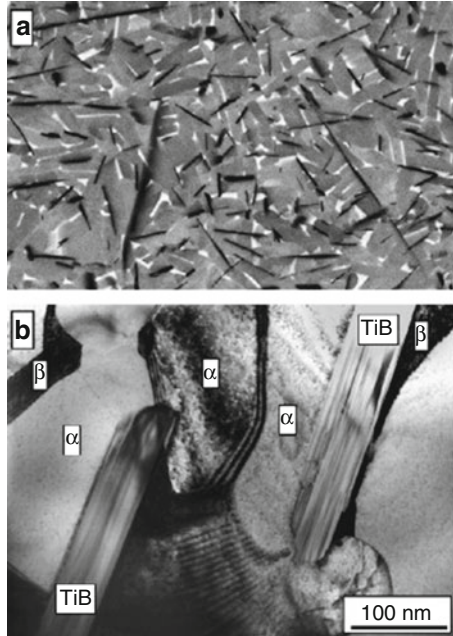
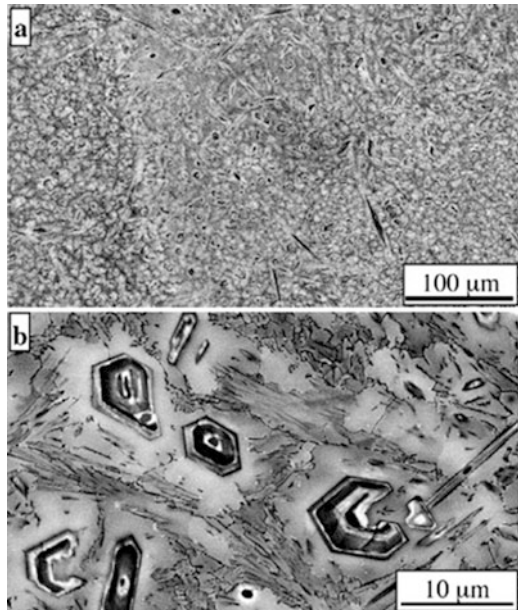


**Fig. 12** (a) Lower magnification and (b) higher magnification backscatter SEM images of LENS™ as-deposited TNZT+2B alloy composites showing both coarser primary borides exhibiting contrast within the same boride precipitate as well as finer scale eutectic borides. (Reprinted with permission from [62])



corrosion resistance and biocompatible properties. However, titanium alloys suffer from rather poor surface hardness and wear resistance properties. One way of improving the hardness as well as tribological properties of titanium alloys is by reinforcing the soft matrix with hard precipitates, such as titanium nitrides, carbides, and borides. These reinforcements can be introduced either via direct incorporation of such hard compounds in the matrix during processing, or via *in situ* reaction with solid or gaseous precursors, resulting the formation of hard precipitates as well as via surface engineering techniques such as nitriding. Focusing on nitride reinforced titanium alloys, the most commonly used technique is surface nitridation of these alloys via heating at elevated temperatures in a flowing nitrogen atmosphere. Another approach that has been employed is the direct introduction of  $\delta$ -TiN and TiB particles during laser deposition of Ti-6Al-4 V. The forming processing approach, nitridation in a gaseous atmosphere, has been applied to the case of  $\beta$  Ti-Mo alloys, resulting in the formation of a continuous surface  $\delta$ -TiN layer and a sub-surface microstructure consisting of laths (or plates) of either the same  $\delta$ -TiN phase or a nitrogen rich  $\alpha$ (Ti, N) solid solution phase, dispersed within the  $\beta$  matrix. While such surface nitridation via heating in a nitrogen atmosphere is a simple and inexpensive way to achieve a case-hardened layer, the time required and the depth of penetration are rather limited and it is difficult to introduce hard nitrides (or other nitrogen enriched hard phases) within the bulk of the material. The direct introduction of nitride and boride particles during laser deposition of titanium alloy powders can obviate this problem. However, the quality of such an interface between such externally introduced reinforcements and the alloy matrix can be rather difficult to control and therefore ideally a reinforcement created as a product of an *in-situ* reaction offers the advantage of a thermodynamically stable and clean interface with the matrix. Furthermore, by employing an *in-situ* nitride (or nitrogen enriched hard  $\alpha$  phase) formation reaction, a more uniform and homogeneous distribution of the nitride phase can be potentially achieved throughout the matrix. *In situ* nitridation during laser deposition of titanium-molybdenum alloys from elemental powder blends has been achieved by introducing the reactive nitrogen gas during the deposition process. Ti-Mo-N alloys have been deposited using the laser engineered net shaping (LENS<sup>TM</sup>) process and resulted in the formation of a hard  $\alpha$ (Ti,N) phase, exhibiting a dendritic morphology, distributed within a  $\beta$ (Ti-Mo) matrix with fine scale transformed  $\alpha$  precipitates. Varying the composition of the Ar + N<sub>2</sub> gas employed during laser deposition permits a systematic increase in the nitrogen content of the as-deposited Ti-Mo-N alloy. Interestingly, the addition of nitrogen, which stabilizes the  $\alpha$  phase in Ti, changes the solidification pathway and the consequent sequence of phase evolution in these alloys. The nitrogen enriched hcp  $\alpha$ (Ti,N) phase has higher *c/a* ratio, exhibits an equiaxed morphology, and tends to form in clusters separated by ribs of the molybdenum (Mo) rich  $\beta$  phase. The Ti-Mo-N alloys also exhibit a substantial enhancement in microhardness due to the formation of these  $\alpha$ (Ti,N) phase, combining it with the desirable properties of the  $\beta$ -Ti matrix, such as excellent ductility, toughness, and formability. All Ti-Mo-N alloys were deposited inside a glove box of LENS<sup>TM</sup> machine with controlled gas atmosphere. Pure Ar (Alloy 1), 25% N<sub>2</sub>-75% Ar (Alloy 2), 50% N<sub>2</sub>-50%Ar (Alloy 3) and

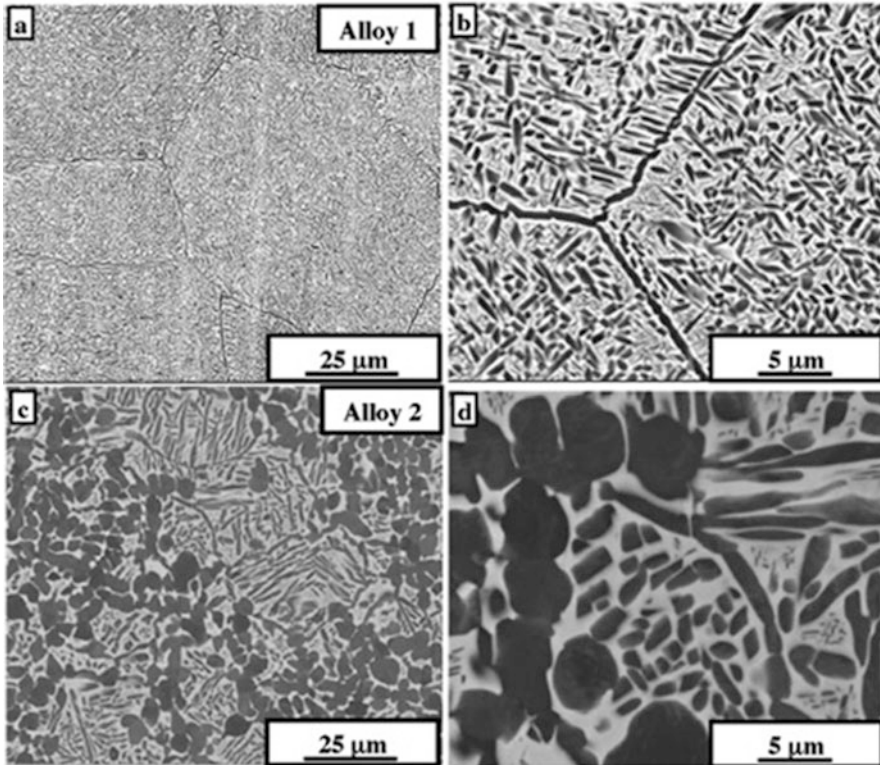


**Fig. 13** (a) Low and (b) high magnification backscatter SEM image of LENS deposited Alloy 1. (c) Low and (d) high magnification backscatter SEM image of LENS deposited Alloy 2. (Reprinted with permission from [5])

75% N<sub>2</sub>-25% Ar (Alloy 4) were the atmospheres used for fabrication of deposits. A series of backscattered SEM images recorded from the Ti-Mo-N alloys are shown in Figs. 13 and 14. Figure 13a, b show the microstructure for the binary Ti-Mo alloy deposited in 100% argon (Ar) atmosphere. The nominal composition of this alloy measured using energy dispersive spectroscopy (EDS) in the SEM is Ti-10wt%Mo. The microstructure primarily consists of uniformly distributed fine scale precipitates of a second phase, presumably  $\alpha$  precipitates, exhibiting a bimodal size distribution within the  $\beta$ -matrix. This bimodal size distribution of  $\alpha$  precipitates can be rationalized on the basis of a two-step decomposition of the  $\beta$ -matrix, wherein the coarser  $\alpha$  precipitates presumably result from the deposition of the layer during LENS<sup>TM</sup> processing, while solid-state re-heating of the same layer, when the subsequent layer is being deposited on the top, results in the secondary decomposition of  $\beta$  forming the finer scale  $\alpha$ . The inherent rapid cooling rates involved in laser deposition, also contribute to such non-equilibrium  $\beta$  decomposition processes. Thus, while during laser deposition of a layer, the phase evolution follows the sequence liquid to  $\beta$  to  $\beta + \alpha$ , the inherently rapid cooling rates involved do not result in an

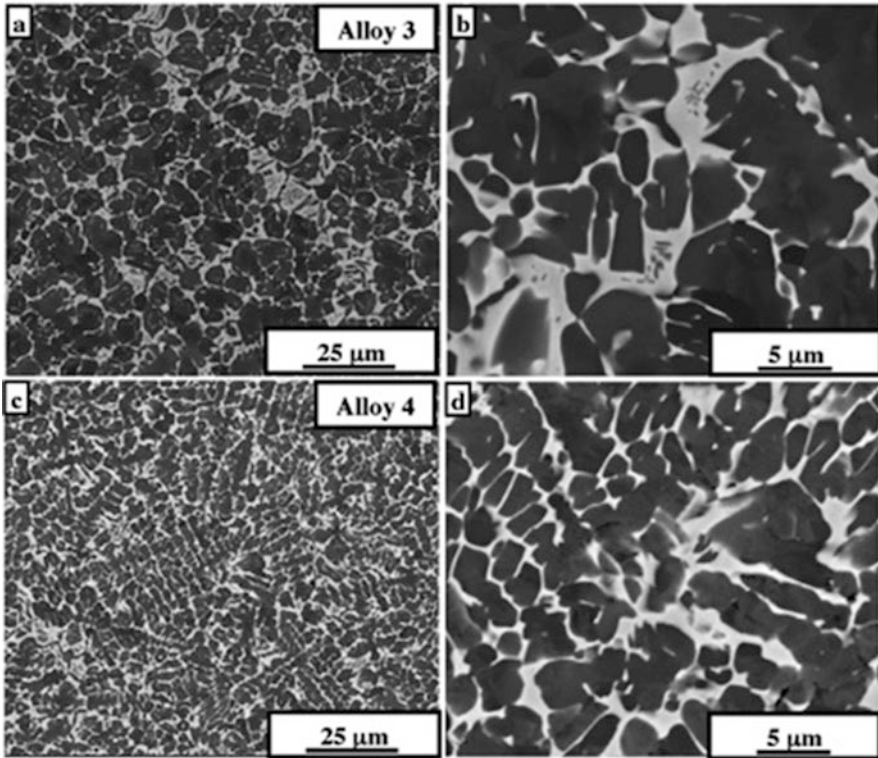


**Fig. 14** (a) Low and (b) high magnification backscatter SEM image of LENS deposited Alloy 3. (c) Low and (d) high magnification backscatter SEM image of LENS deposited Alloy 4. (Reprinted with permission from [5])

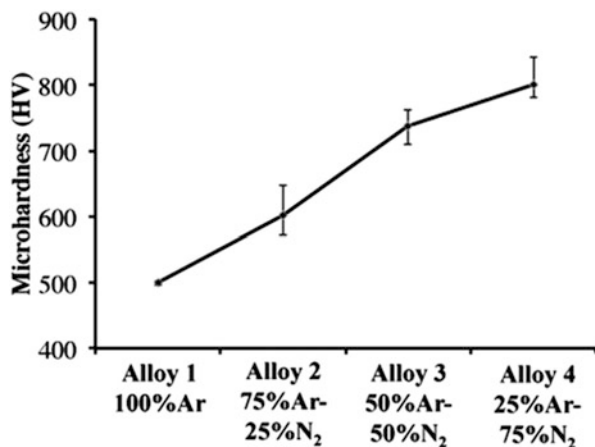
equilibrium composition of the  $\beta$  matrix. Therefore, on subsequent re-heating of the same layer when a layer on top is being deposited, there is a further decomposition of the retained  $\beta$  matrix to form fine scale secondary  $\alpha$  precipitates. The aspect ratio of this finer scale  $\alpha$  is substantially larger than those of the coarser  $\alpha$  precipitates. Figure 13c, d show the microstructure of the Ti-Mo-N alloy deposited using a 75% Ar-25% N<sub>2</sub> atmosphere in the LENS<sup>TM</sup> glovebox as well as the center gas purge and the powder carrier gas. The microstructure clearly exhibits two precipitate phases having rather different morphologies. The coarser precipitates appear to exhibit an equiaxed or globular morphology with curved interfaces separating them from the  $\beta$  matrix, suggesting that these interfaces are presumably incoherent in nature. In contrast, the finer scale precipitates exhibit a sharper faceted morphology suggesting that the precipitate/matrix interface is likely to be semi-coherent. The identity of these two types of precipitates cannot be determined based solely on the backscatter SEM evidence presented in Fig. 13c, d. However, the morphology and contrast of the finer scale precipitates suggests that the  $\alpha$  precipitates exhibited smaller aspect ratios when compared with those observed in case of the binary Ti-10Mo alloy

deposited under a pure Ar atmosphere (Fig. 13a, b). As the  $N_2$  content in the Ar +  $N_2$  mixture used in LENS<sup>TM</sup> deposition increases, the size and volume fraction of the coarser equiaxed second phase precipitates increases significantly in the microstructure, as revealed in Fig. 14. Backscattered scanning electron microscope images of Ti-10Mo alloys LENS<sup>TM</sup> deposited under a 50% Ar-50% $N_2$  mixture are shown in Fig. 14a, b while Fig. 14c, d correspond to an alloy deposited under a 25% Ar-75%  $N_2$  mixture. There is also a corresponding decrease in the  $\beta$  volume fraction with increasing  $N_2$  content in the gaseous atmosphere used for deposition. Thus, the primary microstructural influence of introducing nitrogen during laser deposition appears to be the formation of a novel equiaxed precipitates within the  $\beta$  matrix together with finer scale  $\alpha$  precipitates, with the volume fraction of the equiaxed precipitates increasing with increasing nitrogen content in the alloy.

The Vickers microhardness values for all the four alloys, 1–4, have been plotted in Fig. 15. A systematic increase in the microhardness values, with increasing nitrogen content in the alloys can be clearly observed. The binary Ti-Mo alloy, LENS<sup>TM</sup> deposited under a pure Ar atmosphere, exhibits an average hardness of  $\sim 500$  HV. The increase in microhardness of the Ti-Mo-N alloys, with increasing  $N_2$  content in the reactive atmosphere during LENS<sup>TM</sup> deposition, can be attributed to the formation of the  $\alpha$ -TiN<sub>0.3</sub> random solid solution hexagonal close packed (hcp) phase. For the highest nitrogen containing alloy 4, the microhardness value is  $\sim 800$  HV, which is  $\sim 60\%$  higher as compared with the LENS<sup>TM</sup> deposited binary Ti-10wt%Mo (alloy 1).

In situ nitridation of Ti-10wt%Mo alloys has been achieved by the introduction of reactive nitrogen gas during the laser deposition (LENS<sup>TM</sup>) of these alloys from elemental powder blends. The nitrogen content in these laser deposited alloys has been tuned via changing the ratio of argon to nitrogen used in LENS<sup>TM</sup> deposition. The enrichment of these alloys with nitrogen results in the formation of primary precipitates of the  $\alpha$ (Ti,N) phase within the  $\beta$  matrix. The higher c/a ratio of these hcp  $\alpha$ (Ti,N) precipitates, coupled with the Mo enrichment in the  $\beta$  matrix, results in a

**Fig. 15** A plot showing the variation in Vickers microhardness values for LENS deposited Ti-Mo-N alloys (Alloy 1 to 4). (Reprinted with permission from [5])



substantially large misfit, consequently leading to a loss of precipitate/matrix coherency during growth and coarsening. This results in the  $\alpha(\text{Ti,N})$  precipitates adopting an equiaxed morphology, and they tend to aggregate into clusters separated by thin Mo-rich  $\beta$  ribs. These  $\alpha(\text{Ti,N})$  precipitates increase the microhardness of the alloy to a substantial degree. Additional fine scale secondary  $\alpha$  precipitates, exhibiting a lath or plate-like morphology are also formed within the retained  $\beta$  matrix of these Ti-Mo-N alloys. The ability to introduce controlled volume fractions of the hard nitrogen enriched  $\alpha(\text{Ti,N})$  phase can be very useful in tailoring the local microhardness and consequently wear resistance of these alloys. Furthermore, using the LENS<sup>TM</sup> process it is possible to grade the nitrogen content within the same alloy and thus process a compositionally-graded microstructure with systematically varying properties.

### 2.2.2 Ti64/TNZT-N

Among different metallic alloys, titanium alloys have wide application in industries from orthopedic implants in biomedical to turbine gas engines in aerospace because of their high strength to weight ratio, formability and corrosion resistance [5]. However, they have poor wear resistance. In order to overcome this, titanium alloys need surface treatment such as surface nitridation to improve their wear performance [58]. During surface nitriding, the chemically inert layer is produced in a temperature between (700–1100 °C) in a nitrogen enriched atmosphere [65–74]. Toughness and damage resistance of titanium alloys significantly increases when reinforcement with carbides, nitrides or borides and become potential candidates for industrial utilization [5, 75]. In situ gas reaction in comparison to externally introduced reinforcement has the advantage of mechanically and thermodynamically stability as well as more uniform distribution of reinforcement particles through the alloy matrix [62, 74]. Hamid et al. have processed in situ nitridation of titanium alloys (TNZT and Ti64 alloys) via LENS<sup>TM</sup> process. The backscattered SEM images of Ti64 and nitrided Ti64 alloys are shown in Fig. 16. The Ti64 alloys exhibit typical  $\alpha$ - $\beta$  microstructure whereas nitrided Ti64 shows presence of 2 types of equiaxed- $\alpha$  laths with smaller aspect ratio. The typical dendritic microstructures have been observed in LENS<sup>TM</sup> deposited TNZT alloys (Fig. 17a) whereas darker dendritic TiN/TiN<sub>2</sub> precipitates have been observed in nitrided TNZT composites (Fig. 17b). The cross-sectional STEM-HADF image along with EDS elemental map of nitrided TNZT is shown in Fig. 17c, where  $\beta$  matrix enriched in Nb and Ta and  $\alpha$  precipitates are deficient in Nb and Ta. The microhardness results of the LENS<sup>TM</sup> deposited Ti64, TNZT, and nitrided Ti64 and TNZT are summarized in Fig. 18. Ti64 has a higher hardness compared to Ti-Nb-Zr-Ta mainly due to the presence of mixed  $\alpha$ - $\beta$  microstructure. Both nitrided Ti64 and TNZT exhibits higher microhardness than base alloys mainly due to the presence of TiN/Ti<sub>2</sub>N precipitates in Ti-Nb-Zr-Ta, and the nitrogen-enriched  $\alpha$  phase in Ti64 alloys.

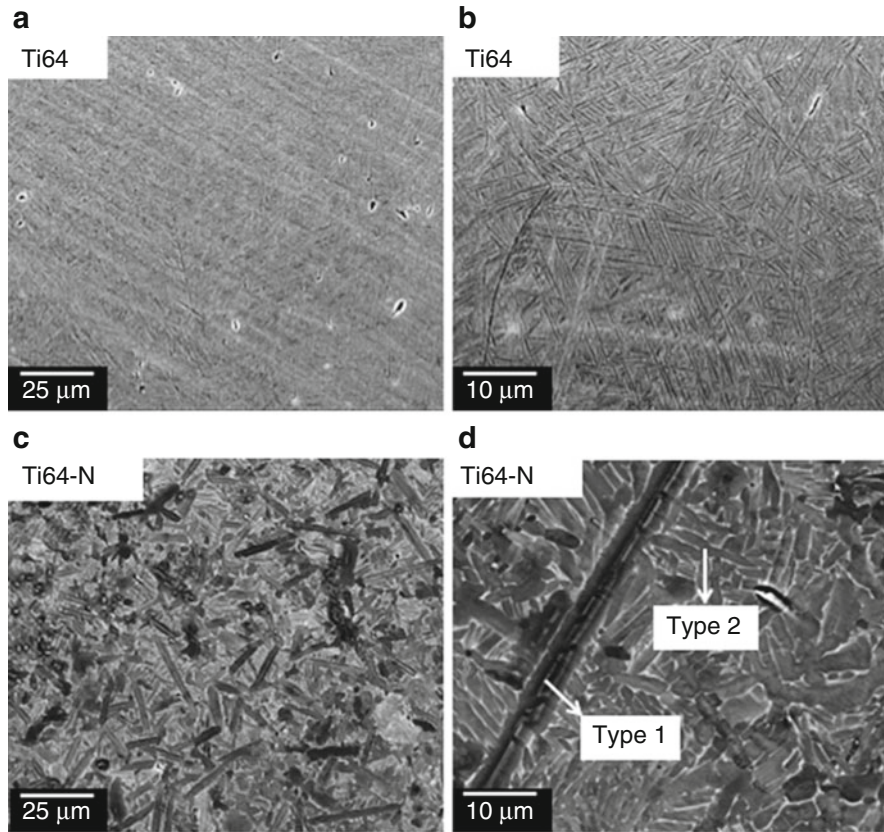


**Fig. 16** (a) Low- and (b) high-magnification backscatter SEM images of LENS deposited Ti64 alloy. (c) Low- and (d) high-magnification backscatter SEM images of LENS deposited nitrided Ti64 (Ti64-N) alloy. (Reprinted with permission from [74])

### 3 Summary

Laser additive manufacturing of in situ metal matrix composites offers various advantages as compared to the conventional processing and also has capability to produce near-net shape components. This chapter provided the overview of laser additive manufacturing of in situ metal matrix. Broadly, two types of in situ reactions have been discussed: in situ reaction between elemental blend powder and in situ reaction between elemental blend powder and reactive gases. In situ Aluminum matrix composites processed via selective laser melting (SLM) process have shown significant improvement in hardness, tribological and mechanical properties as compared to their base alloy. Laser additively manufactured in situ nickel-titanium-graphite composites have shown significant improvement in microhardness as well as tribological properties as compared to pure nickel and is potential candidate for

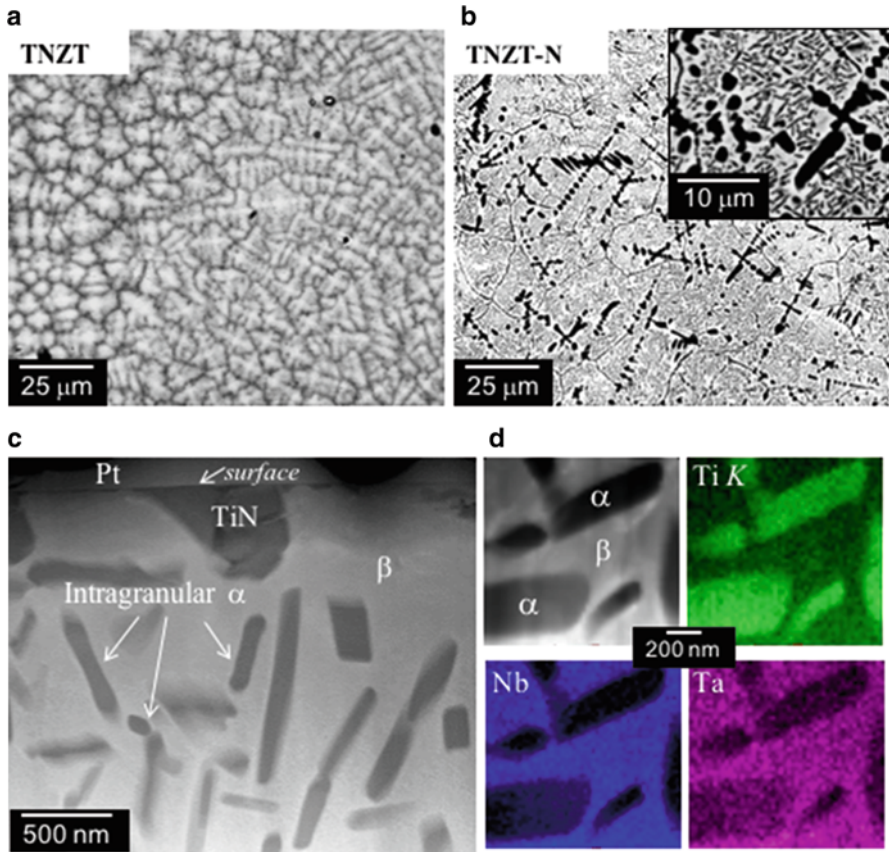
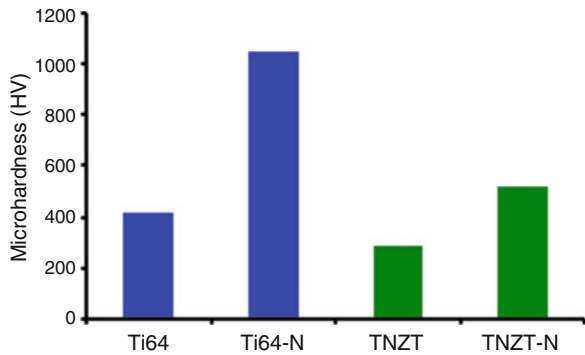


**Fig. 17** Low-magnification backscatter SEM images of LENS deposited (a) TNZT and (b) nitrided TNZT (TNZT-N) alloys. (c) Cross-sectional HAADF-STEM image of nitrided TNZT alloy with corresponding titanium, niobium and tantalum EDS maps. (Reprinted with permission from [74])

**Fig. 18** Plot showing the variation in Vickers microhardness values for LENS deposited Ti64, Ti64-N, TNZT, and TNZT-N alloys





high temperature surface engineering applications. In situ titanium alloys composites have shown improvement in wear properties and ideal for biomedical applications.

## References

1. I. Gibson, D. W. Rosen, and B. Stucker, *Additive manufacturing technologies: Rapid prototyping to direct digital manufacturing*. 2010.
2. N. Guo and M. C. Leu, "Additive manufacturing: Technology, applications and research needs," *Frontiers of Mechanical Engineering*, vol. 8, no. 3, pp. 215–243, 2013.
3. T. Borkar *et al.*, "A combinatorial assessment of AlxCrCuFeNi<sub>2</sub> (0)," *Acta Mater.*, vol. 116, pp. 63–76, 2016.
4. T. Borkar *et al.*, "Laser-deposited in situ TiC-reinforced nickel matrix composites: 3D microstructure and tribological properties," *JOM*, vol. 66, no. 6, pp. 935–942, 2014.
5. T. Borkar, S. Gopagani, S. Nag, J. Y. Hwang, P. C. Collins, and R. Banerjee, "In situ nitridation of titanium-molybdenum alloys during laser deposition," *J. Mater. Sci.*, vol. 47, no. 20, pp. 7157–7166, 2012.
6. T. Borkar, R. Conteri, X. Chen, R. V. Ramanujan, and R. Banerjee, "Laser additive processing of functionally-graded Fe–Si–B–Cu–Nb soft magnetic materials," *Mater. Manuf. Process.*, vol. 32, no. 14, pp. 1581–1587, 2017.
7. C. V. Mikler *et al.*, "Laser Additive Manufacturing of Magnetic Materials," *JOM*, vol. 69, no. 3, pp. 532–543, 2017.
8. W. J. Sames, F. A. List, S. Pannala, R. R. Dehoff, and S. S. Babu, "The metallurgy and processing science of metal additive manufacturing," *International Materials Reviews*, vol. 61, no. 5, pp. 315–360, 2016.
9. W. E. Frazier, "Metal additive manufacturing: A review," *Journal of Materials Engineering and Performance*, vol. 23, no. 6, pp. 1917–1928, 2014.
10. J. C. Zhao, "Combinatorial approaches as effective tools in the study of phase diagrams and composition-structure-property relationships," *Prog. Mater. Sci.*, vol. 51, no. 5, pp. 557–631, 2006.
11. S. Curtarolo, G. L. W. Hart, M. B. Nardelli, N. Mingo, S. Sanvito, and O. Levy, "The high-throughput highway to computational materials design," *Nat. Mater.*, vol. 12, no. 3, pp. 191–201, 2013.
12. D. D. Gu, W. Meiners, K. Wissenbach, and R. Poprawe, "Laser additive manufacturing of metallic components: materials, processes and mechanisms," *Int. Mater. Rev.*, vol. 57, no. 3, pp. 133–164, 2012.
13. P. A. Kobryn and S. L. Semiatin, "The laser additive manufacture of Ti-6Al-4V," *JOM*, vol. 53, no. 9, pp. 40–42, 2001.
14. Y. J. Liang, D. Liu, and H. M. Wang, "Microstructure and mechanical behavior of commercial purity Ti/Ti-6Al-2Zr-1Mo-1V structurally graded material fabricated by laser additive manufacturing," *Scr. Mater.*, vol. 74, pp. 80–83, 2014.
15. D. C. Hofmann *et al.*, "Compositionally graded metals: A new frontier of additive manufacturing," *J. Mater. Res.*, vol. 29, no. 17, pp. 1899–1910, 2014.
16. D. C. Hofmann *et al.*, "Developing gradient metal alloys through radial deposition additive manufacturing," *Sci. Rep.*, vol. 4, 2014.
17. T. Wohlers and T. Caffrey, *Wohlers Report 2015: 3D Printing and Additive Manufacturing State of the Industry Annual Worldwide Progress Report*. 2014.
18. E. C. Santos, M. Shiomi, K. Osakada, and T. Laoui, "Rapid manufacturing of metal components by laser forming," *Int. J. Mach. Tools Manuf.*, vol. 46, no. 12–13, pp. 1459–1468, 2006.
19. P. Heinl, A. Rottmair, C. Körner, and R. F. Singer, "Cellular titanium by selective electron beam melting," *Adv. Eng. Mater.*, vol. 9, no. 5, pp. 360–364, 2007.

20. J.-P. Kruth, P. Mercelis, J. Vaerenbergh, L. Froyen, and M. Rombouts, "Binding mechanisms in selective laser sintering and selective laser melting," *Rapid Prototyp. J.*, vol. 11, no. 1, pp. 26–36, 2005.
21. I. Zein, D. W. Huttmacher, K. C. Tan, and S. H. Teoh, "Fused deposition modeling of novel scaffold architectures for tissue engineering applications," *Biomaterials*, vol. 23, no. 4, pp. 1169–1185, 2002.
22. F. Abe, K. Osakada, M. Shiomi, K. Uematsu, and M. Matsumoto, "The manufacturing of hard tools from metallic powders by selective laser melting," *J. Mater. Process. Technol.*, vol. 111, no. 1–3, pp. 210–213, 2001.
23. B. Vandenbroucke and J. Kruth, "Selective laser melting of biocompatible metals for rapid manufacturing of medical parts," *Rapid Prototyp. J.*, vol. 13, no. 4, pp. 196–203, 2007.
24. L. Thijs, F. Verhaeghe, T. Craeghs, J. Van Humbeeck, and J. P. Kruth, "A study of the microstructural evolution during selective laser melting of Ti-6Al-4V," *Acta Mater.*, vol. 58, no. 9, pp. 3303–3312, 2010.
25. N. Shamsaei, A. Yadollahi, L. Bian, and S. M. Thompson, "An overview of Direct Laser Deposition for additive manufacturing; Part II: Mechanical behavior, process parameter optimization and control," *Addit. Manuf.*, vol. 8, pp. 12–35, 2015.
26. R. Morgan, C. J. Sutcliffe, and W. O'Neill, "Density analysis of direct metal laser re-melted 316L stainless steel cubic primitives," *J. Mater. Sci.*, vol. 39, no. 4, pp. 1195–1205, 2004.
27. J. P. Kruth, G. Levy, F. Klocke, and T. H. C. Childs, "Consolidation phenomena in laser and powder-bed based layered manufacturing," *CIRP Ann. - Manuf. Technol.*, vol. 56, no. 2, pp. 730–759, 2007.
28. I. A. Ibrahim, F. A. Mohamed, and E. J. Lavernia, "Particulate reinforced metal matrix composites - a review," *Journal of Materials Science*, vol. 26, no. 5, pp. 1137–1156, 1991.
29. A. P. Divecha, S. G. Fishman, and S. D. Karmarkar, "Silicon Carbide Reinforced Aluminum—A Formable Composite," *JOM J. Miner. Met. Mater. Soc.*, vol. 33, no. 9, pp. 12–17, 1981.
30. P. Sahoo and M. J. Koczak, "Microstructure-property relationships of in situ reacted TiC/AlCu metal matrix composites," *Mater. Sci. Eng. A*, vol. 131, no. 1, pp. 69–76, 1991.
31. S. Dadbakhsh and L. Hao, "In situ formation of particle reinforced Al matrix composite by selective laser melting of Al/Fe<sub>2</sub>O<sub>3</sub> powder mixture," *Adv. Eng. Mater.*, vol. 14, no. 1–2, pp. 45–48, 2012.
32. Z. Zhong and N. P. Hung, "Grinding of alumina/aluminum composites," *J. Mater. Process. Technol.*, vol. 123, no. 1, pp. 13–17, 2002.
33. S. J. Zhu and T. Iizuka, "Fabrication and mechanical behavior of Al matrix composites reinforced with porous ceramic of in situ grown whisker framework," *Mater. Sci. Eng. A*, vol. 354, no. 1–2, pp. 306–314, 2003.
34. E. J. Lavernia, J. D. Ayers, and T. S. Srivatsan, "Rapid solidification processing with specific application to aluminium alloys," *Int. Mater. Rev.*, vol. 37, no. 1, pp. 1–44, 1992.
35. E. J. Lavernia and T. S. Srivatsan, "The rapid solidification processing of materials: Science, principles, technology, advances, and applications," *Journal of Materials Science*, vol. 45, no. 2, pp. 287–325, 2010.
36. S. Dadbakhsh, L. Hao, P. G. E. Jerrard, and D. Z. Zhang, "Experimental investigation on selective laser melting behaviour and processing windows of in situ reacted Al/Fe<sub>2</sub>O<sub>3</sub> powder mixture," *Powder Technol.*, vol. 231, pp. 112–121, 2012.
37. R. H. Fan, H. L. Lü, K. N. Sun, W. X. Wang, and X. B. Yi, "Kinetics of thermite reaction in Al-Fe<sub>2</sub>O<sub>3</sub> system," *Thermochim. Acta*, vol. 440, no. 2, pp. 129–131, 2006.
38. M. Das, V. K. Balla, D. Basu, S. Bose, and A. Bandyopadhyay, "Laser processing of SiC-particle-reinforced coating on titanium," *Scr. Mater.*, vol. 63, no. 4, pp. 438–441, 2010.
39. R. Anandkumar, A. Almeida, and R. Vilar, "Wear behavior of Al-12Si/TiB<sub>2</sub> coatings produced by laser cladding," *Surf. Coatings Technol.*, vol. 205, no. 13–14, pp. 3824–3832, 2011.
40. J. M. Torralba, C. E. Da Costa, and F. Velasco, "P/M aluminum matrix composites: An overview," *Journal of Materials Processing Technology*, vol. 133, no. 1–2, pp. 203–206, 2003.

41. D. Gu, F. Chang, and D. Dai, "Selective Laser Melting Additive Manufacturing of Novel Aluminum Based Composites With Multiple Reinforcing Phases," *J. Manuf. Sci. Eng.*, vol. 137, no. 2, p. 21010, 2015.
42. X. S. Cong, P. Shen, Y. Wang, and Q. Jiang, "Wetting of polycrystalline SiC by molten Al and Al-Si alloys," *Appl. Surf. Sci.*, vol. 317, pp. 140–146, 2014.
43. C. Xue and J. K. Yu, "Enhanced thermal transfer and bending strength of SiC/Al composite with controlled interfacial reaction," *Mater. Des.*, vol. 53, pp. 74–78, 2014.
44. A. Simchi and D. Godlinski, "Effect of SiC particles on the laser sintering of Al-7Si-0.3Mg alloy," *Scr. Mater.*, vol. 59, no. 2, pp. 199–202, 2008.
45. E. Louvis, P. Fox, and C. J. Sutcliffe, "Selective laser melting of aluminium components," *J. Mater. Process. Technol.*, vol. 211, no. 2, pp. 275–284, 2011.
46. F. Chang, D. Gu, D. Dai, and P. Yuan, "Selective laser melting of in-situ Al<sub>4</sub>SiC<sub>4</sub> + SiC hybrid reinforced Al matrix composites: Influence of starting SiC particle size," *Surf. Coatings Technol.*, vol. 272, pp. 15–24, 2015.
47. A. L. Patterson, "The scherrer formula for X-ray particle size determination," *Phys. Rev.*, vol. 56, no. 10, pp. 978–982, 1939.
48. J. P. Kruth, X. Wang, T. Laoui, and L. Froyen, "Lasers and materials in selective laser sintering," *Assem. Autom.*, vol. 23, no. 4, pp. 357–371, 2003.
49. S. Gopagoni *et al.*, "Microstructural evolution in laser deposited nickel-titanium-carbon in situ metal matrix composites," *J. Alloys Compd.*, vol. 509, no. 4, pp. 1255–1260, 2011.
50. Z. de Liu, J. Tian, B. Li, and L. ping Zhao, "Microstructure and mechanical behaviors of in situ TiC particulates reinforced Ni matrix composites," *Mater. Sci. Eng. A*, vol. 527, no. 16–17, pp. 3898–3903, 2010.
51. D. Strzȩciwilk, Z. Wokulski, and P. Tkacz, "Microstructure of TiC crystals obtained from high temperature nickel solution," *J. Alloys Compd.*, vol. 350, no. 1–2, pp. 256–263, 2003.
52. G. Xiao, Q. Fan, M. Gu, Z. Wang, and Z. Jin, "Dissolution-precipitation mechanism of self-propagating high-temperature synthesis of TiC-Ni cermet," *Mater. Sci. Eng. A*, vol. 382, no. 1–2, pp. 132–140, 2004.
53. Y. Li, P. Bai, Y. Wang, J. Hu, and Z. Guo, "Effect of TiC content on Ni/TiC composites by direct laser fabrication," *Mater. Des.*, vol. 30, no. 4, pp. 1409–1412, 2009.
54. D. Strzȩciwilk, P. Tkacz, and Z. Wokulski, "Transmission electron microscope studies of TiC crystals," *Cryst. Res. Technol.*, vol. 35, no. 11–12, pp. 1295–1303, 2000.
55. H. Sahasrabudhe, J. Soderlind, and A. Bandyopadhyay, "In Situ Nitridation of Titanium Using Lens™," *Biomaterials Science: Processing, Properties and Applications V: Ceramic Transactions, Volume 254*, pp. 149–159, 2015.
56. H. Sahasrabudhe, J. Soderlind, and A. Bandyopadhyay, "Laser processing of in situ TiN/Ti composite coating on titanium," *J. Mech. Behav. Biomed. Mater.*, vol. 53, pp. 239–249, 2016.
57. M. Das, V. K. Balla, D. Basu, I. Manna, T. S. Sampath Kumar, and A. Bandyopadhyay, "Laser processing of in situ synthesized TiB-TiN-reinforced Ti6Al4V alloy coatings," *Scr. Mater.*, vol. 66, no. 8, pp. 578–581, 2012.
58. M. Das *et al.*, "In situ synthesized TiB-TiN reinforced Ti6Al4V alloy composite coatings: Microstructure, tribological and in-vitro biocompatibility," *J. Mech. Behav. Biomed. Mater.*, vol. 29, pp. 259–271, 2014.
59. H. Attar, M. Bönisch, M. Calin, L. C. Zhang, S. Scudino, and J. Eckert, "Selective laser melting of in situ titanium-titanium boride composites: Processing, microstructure and mechanical properties," *Acta Mater.*, vol. 76, pp. 13–22, 2014.
60. V. K. Balla, W. Xue, S. Bose, and A. Bandyopadhyay, "Laser-assisted Zr/ZrO<sub>2</sub> coating on Ti for load-bearing implants," *Acta Biomater.*, vol. 5, no. 7, pp. 2800–2809, 2009.
61. R. Banerjee, P. C. Collins, and H. L. Fraser, "Laser Deposition of In Situ Ti – TiB Composites," *Adv. Eng. Mater.*, vol. 4, no. 11, pp. 847–851, 2002.
62. S. Samuel, S. Nag, T. W. Scharf, and R. Banerjee, "Wear resistance of laser-deposited boride reinforced Ti-Nb-Zr-Ta alloy composites for orthopedic implants," *Mater. Sci. Eng. C*, vol. 28, no. 3, pp. 414–420, 2008.

63. S. Nag, S. Samuel, A. Puthucode, and R. Banerjee, "Characterization of novel borides in Ti-Nb-Zr-Ta + 2B metal-matrix composites," *Mater. Charact.*, vol. 60, no. 2, pp. 106–113, 2009.
64. A. Genç, R. Banerjee, D. Hill, and H. L. Fraser, "Structure of TiB precipitates in laser deposited in situ, Ti-6Al-4V-TiB composites," *Mater. Lett.*, vol. 60, no. 7, pp. 859–863, 2006.
65. D. G. Bansal, O. L. Eryilmaz, and P. J. Blau, "Surface engineering to improve the durability and lubricity of Ti-6Al-4V alloy," *Wear*, vol. 271, no. 9–10, pp. 2006–2015, 2011.
66. M. Geetha, A. K. Singh, R. Asokamani, and A. K. Gogia, "Ti based biomaterials, the ultimate choice for orthopaedic implants - A review," *Progress in Materials Science*, vol. 54, no. 3, pp. 397–425, 2009.
67. A. Liu, "Transcendental Data: Toward a Cultural History and Aesthetics of the New Encoded Discourse," *Crit. Inq.*, vol. 31, no. Autumn, pp. 49–84, 2004.
68. R. A. Buchanan, E. D. Rigney, and J. M. Williams, "Ion implantation of surgical Ti-6Al-4V for improved resistance to wear-accelerated corrosion," *J. Biomed. Mater. Res.*, vol. 21, no. 3, pp. 355–366, 1987.
69. C. B. Johansson, J. Lausmaa, T. Röstlund, and P. Thomsen, "Commercially pure titanium and Ti-6Al-4V implants with and without nitrogen-ion implantation: surface characterization and quantitative studies in rabbit cortical bone," *J. Mater. Sci. Mater. Med.*, vol. 4, no. 2, pp. 132–141, 1993.
70. C. Hu, H. Xin, L. M. Watson, and T. N. Baker, "Analysis of the phases developed by laser nitriding Ti-6Al-4V alloys," *Acta Mater.*, vol. 45, no. 10, pp. 4311–4322, 1997.
71. A. Czyska-Filemonowicz *et al.*, "Transmission electron microscopy and atomic force microscopy characterisation of titanium-base alloys nitrided under glow discharge," *Acta Mater.*, vol. 53, no. 16, pp. 4367–4377, 2005.
72. A. Zhecheva, W. Sha, S. Malinov, and A. Long, "Enhancing the microstructure and properties of titanium alloys through nitriding and other surface engineering methods," *Surface and Coatings Technology*, vol. 200, no. 7, pp. 2192–2207, 2005.
73. M. Nakai *et al.*, "Surface hardening of biomedical Ti-29Nb-13Ta-4.6Zr and Ti-6Al-4V ELI by gas nitriding," *Mater. Sci. Eng. A*, vol. 486, no. 1–2, pp. 193–201, 2008.
74. H. Mohseni, P. Nandwana, A. Tsoi, R. Banerjee, and T. W. Scharf, "In situ nitrided titanium alloys: Microstructural evolution during solidification and wear," *Acta Mater.*, vol. 83, pp. 61–74, 2015.
75. R. Banerjee, P. C. Collins, A. Genç, and H. L. Fraser, "Direct laser deposition of in situ Ti-6Al-4V-TiB composites," *Mater. Sci. Eng. A*, vol. 358, no. 1–2, pp. 343–349, 2003.